Investigation of energy absorption capacity of 3D filament wound composite tubes experimental evaluation, numerical simulation, and acoustic emission monitoring

Alimirzaei, Sajad; Ahmadi Najafabadi, Mehdi; Nikbakht, Ali; Pahlavan, Lotfollah

DOI
10.1080/15376494.2022.2163437

Publication date
2023

Document Version
Final published version

Published in
Mechanics of Advanced Materials and Structures

Citation (APA)
Alimirzaei, S., Ahmadi Najafabadi, M., Nikbakht, A., & Pahlavan, L. (2023). Investigation of energy absorption capacity of 3D filament wound composite tubes: experimental evaluation, numerical simulation, and acoustic emission monitoring. *Mechanics of Advanced Materials and Structures*, *31 (2024)*(13), 2727-2742. https://doi.org/10.1080/15376494.2022.2163437

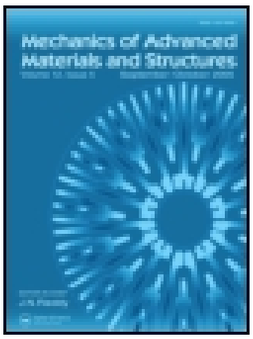

Mechanics of Advanced Materials and Structures

ISSN: (Print) (Online) Journal homepage: https://www.tandfonline.com/loi/umcm20

Investigation of energy absorption capacity of 3D filament wound composite tubes: experimental evaluation, numerical simulation, and acoustic emission monitoring

Sajad Alimirzaei, Mehdi Ahmadi Najafabadi, Ali Nikbakht & Lotfollah Pahlavan

To cite this article: Sajad Alimirzaei, Mehdi Ahmadi Najafabadi, Ali Nikbakht & Lotfollah Pahlavan (2023): Investigation of energy absorption capacity of 3D filament wound composite tubes: experimental evaluation, numerical simulation, and acoustic emission monitoring, Mechanics of Advanced Materials and Structures, DOI: 10.1080/15376494.2022.2163437

To link to this article: https://doi.org/10.1080/15376494.2022.2163437

Published online: 25 Jan 2023.

MECHANICS OF ADVANCED MATERIALS AND STRUCTURES
https://doi.org/10.1080/15376494.2022.2163437

Taylor & Francis
Taylor & Francis Group

ORIGINAL ARTICLE

Investigation of energy absorption capacity of 3D filament wound composite tubes: experimental evaluation, numerical simulation, and acoustic emission monitoring

Sajad Alimirzaei[a,b], Mehdi Ahmadi Najafabadi[a], Ali Nikbakht[b], and Lotfollah Pahlavan[c]

[a]Department of Mechanical Engineering, Amirkabir University of Technology, Tehran, Iran; [b]Technologies Research Center (NTRC), Amirkabir University of Technology, Tehran, Iran; [c]Department of Maritime and Transport Technology, TU Delft, Delft, The Netherlands

ABSTRACT

By analyzing the failure mechanisms, crashworthiness characteristics of FW composite tubes subjected to two modes of progressive damage and catastrophic failure are investigated using acoustic emission technique and numerical method. The AE signals of ±45° composite tubes were classified using hierarchical and wavelet transform methods, and based on the realistic and three-dimensional geometrical architecture of tubular structures, the microstructural finite element model was developed using Catia and ABAQUS software. Then deformation patterns and the impression of each mechanism on the crashworthiness characteristics were assessed. Results indicated that fiber breakage and fiber/matrix debonding could likely control the higher percentage of damage. By changing the type of modes from progressive damage to catastrophic failure, the percentage of matrix cracking increases, the fiber/matrix separation decreases, and the failure behavior become dominated by local buckling. Comparing the FE simulation with experimental results, we found the proposed 3D model can reasonably predict the pre-crushing, post-crushing, and material densification.

ARTICLE HISTORY
Received 16 June 2022
Accepted 24 December 2022

KEYWORDS
Acoustic emission; finite element simulation; filament wound composite tubes; failure modes; clustering method

1. Introduction

Thin-walled structures are widely used in different industries, and substantial efforts have been made to increase their impact energy absorption capacity and improve their safety [1]. Among various types of materials and geometries, fiber-reinforced composite tubes represent a good energy absorbing capability and have great potential as energy-absorbing components to substitute their metallic counterparts in automotive, aerospace, and maritime structures [2, 3]. McGregor et al. [4] developed the progressive damage simulation of braided tubes under compressional loading. They used a user material subroutine model in LS-DYNA software for the simulation of failure mechanisms. The result of this study showed that the ability of the numerical model to the prediction of energy absorption and observed failure morphology correlated well with their experimental results. Gu et al. [5] investigated the failure mechanism and progressive damage of braided composite tubes under torsional loading. They used three-dimensional (3D) digital image correlation (DIC) for monitoring crack propagation in 30°, 45°, 55°, and 60° samples. Their results indicated that the failure modes of 30° and 60° samples were especially dominated by matrix failure, whereas 45° and 50° samples were largely influenced by fiber breakage. Ryzińskaa et al. [6] and Luo et al. [7] investigated the progressive crushing performance of carbon epoxy composite tubes with varied fiber braiding. In these studies, the effect of lay-up configuration on the specific energy absorption (SEA) was investigated. In other research, Luo et al. [8] investigated the failure behavior of pre-embedded coupling of filament wound (FW) composite tubes. Their results showed that in comparison with the bonding joints, the maximum damage load of the samples was higher than 105 kN. Rafiee et al. [9] studied the structural damage of FW composite tubes subjected to internal pressure load. For the prediction of the load-bearing capacity of FW composite tubes, they used progressive damage modeling, and for material degradation, the continuum damage mechanic (CDM) model and ply discount method were used. Shi et al. [10] and Higuchi et al. [11] developed an enhanced CDM approach for crash simulation of composite structures. They employed two submodels, a post-failure model and a pre-failure model, to characterize the stress–strain performance. Esa et al. [12] proposed the piecemeal energy absorption (PEA) capacity as a novel scheme to assess the crashworthiness of composite tubes. Based on the geometrical dimensions of the structure, the PEA strategy generated higher energy absorption under high impact velocity and lower damage under lower impact velocity to improve the crashworthiness of the tube. Belardi et al. [13] investigated the construction analysis of anisogrid lattice shells subject to external loads. They used a discrete method to compute the critical buckling load of the anisogrid lattice construction. Sik et al. [14] developed a procedure

CONTACT M.A. Najafabadi ahmadin@aut.ac.ir Department of Mechanical Engineering, Amirkabir University of Technology, Tehran, Iran.

to model composite structures with the embedded element method and utilized two user material subroutines to implement this method. Results showed that this method is well adaptable for diverse boundary conditions, element types, and the various volume fractions of fibers.

To characterize the different damage mechanisms, the acoustic emission (AE) technique has been found as a promising method in active crack detection [15–19]. Beheshtizaeh and Mostafapour [20] used the AE method for monitoring glass fiber reinforced plastic (GFRP) samples and carbon fiber reinforced plastic (CFRP) samples under flexural loading. Saidane et al. [21] studied the mode-I fracture toughness of hybrid flax-glass, glass, and flax fiber woven composites. They used scanning electron microscope images (SEM) and the AE signals recorded during the tests to analyze the failure mechanism. Ali et al. [22] focused on the failure analysis of woven composites under tensile and flexural loading. They suggested a GAP function to find the optimal clusters of AE data. Huijer et al. [23] investigated the damage mechanisms in CFRP samples during a four-point bending test with AE using embedded piezoelectric sensors. To assess these, two types of piezoelectric wafer active sensors (PWAS) were used. Also, for the identification and clustering of the AE signals, a hierarchical clustering approach was proposed. Ameur et al. [24] investigated the failure mechanisms of unidirectional carbon/flax composites under tensile tests using the AE method. They used the k-means algorithm and obtained four classes of AE events based on temporal classification parameters. Šofer et al. [25] and Khalifa et al. [26] experimentally evaluated the failure mechanisms of composite tubes subject to a three-point bending test and tensile test using AE monitoring, respectively. The results of these studies showed that the damage could be classified into four groups.

Due to the limitations of eye inspection, SEM methods, and numerical methods, it seemed necessary to use a precise technique to gain more detailed insight into the damage mechanisms and, the effect of each mechanism on the energy absorption capacity. This study's aim is to characterize and compare the mechanical behavior of two types of progressive failure and catastrophic failure modes of FW composite tubes employing experimental evaluation, AE monitoring, and numerical simulation. In order to identify the damage mechanisms, machine learning-based methods are used. Then, the results are analyzed using a recognition approach based on the wavelet packet transform (WPT) model and fast Fourier transforms (FFT), and the percentage of damage mechanisms is obtained. Also, an improved approach for modeling the FW composite tubes is proposed for progressive damage analysis of the tubes. The approach includes the accurate generation of 3D filament fiber paths and the overlap between the fibers. The embedded region method is used for the latter. For progressive damage analysis of the tubes, the maximum stress criterion and Hill's yield criterion were written as a user material subroutine in Fortran software, and compiled by ABAQUS^{TM} software. A quantitative assessment of each of these mechanisms can be of great help in understanding how energy is absorbed by the target structure, which could be used to optimize the structures based on the effective damage mechanism.

2. Experimental process

2.1. Influential parameters for energy absorption

The failure mechanisms occurring in composite tubes under axial compressive loading are primarily due to various failure modes including progressive failure mode (mode I), catastrophic failure mode (mode II), and combined failure mode. Research shows that the failure caused by loading in mode I have the highest energy absorption due to the progressive nature of the failure. However, two other modes are mostly catastrophic. After approaching a peak force, it suddenly drops sharply and reduces the mean crushing force and energy absorption of structures [27]. One of the most important parameters in the energy absorption of the composite tubes is the ratio of diameter to thickness (D/t). In small D/t ratios, buckling does not take place, and energy absorption mode is mainly in the form of elastic deformation and compressive crushing [28, 29]. However, with an increasing D/t ratio, buckling mode occurs and the start of buckling prevents the tube from crushing. Studies on optimizing the geometric dimensions of thin-walled cylindrical tubes show that to achieve the maximum energy absorption state, the geometric dimensions of the tubes must be within the $0.015 \prec \frac{t}{D} \prec 0.25$ limits [27].

2.2. Manufacturing of composite tube

Composite tubes were fabricated from carbon/LY5052 epoxy using a filament winding machine (Figure 1a). After curing the FW composite pipes for 24 h at room temperature, composite samples were post-cured at 100 °C for 4 hours in an oven with air circulation. Finally, the fabricated composite pipes were cut with a length of 120 mm, a diameter of 60 mm, and a thickness of 1.5 mm for the axial compression test (Figure 1b). According to the literature, energy absorption can be increased by creating a triggered edge mechanism [30, 31]. This effect can enable the progressive failure mode and increase the energy absorption of the FW tubes. So, a 45-degree chamfer was created at one end of the specimens. More details, including the completely described fabrication process of composite samples, are reported in [32]. Furthermore, to specify the volume fraction of fiber and resin, the burning test was implemented following the ASTM D2584 [33] standard. To do so, the first small pieces of the samples were cut and weighed. Then, the specimens were placed in an oven at 200 °C for 2 h to burn and destroy the composite resin. By weighing the parts after burning the resin, the volume percentage of fiber was calculated as 59.48%.

2.3. Compression tests

Quasi-static compression tests were carried out on samples using an MTS 250 KN hydraulic machine with a speed of 5 mm/min. The AE sensors were broadband piezoelectric with a 34 dB external preamplifier. An eight-channel AE

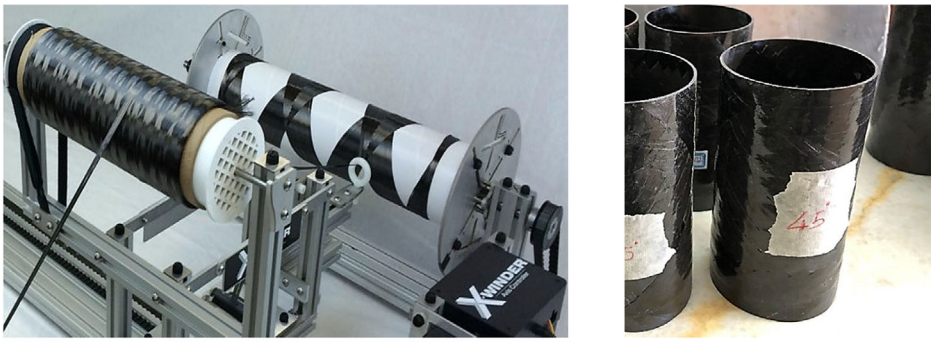

Figure 1. (a) Fabrication of filament wound composite tubes, (b) FW composite tube.

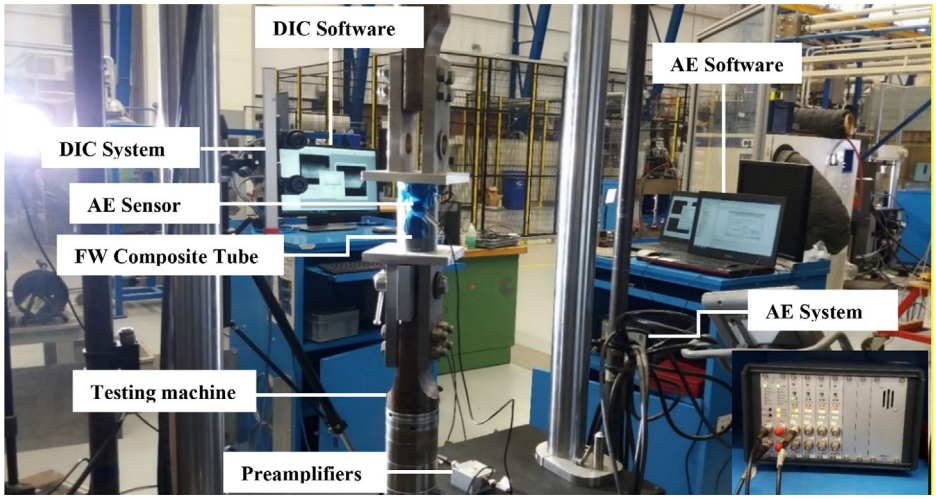

Figure 2. Experimental setup of this study.

AMSY-6 (Vallen System GmbH) system with the operational frequency range of [100–900 kHz] was used to receive the AE signals. The sampling rate and the threshold were set to 2 MHz and 55 dB, respectively. Also, a hit definition time (HDT) and hit lockout time (HLT) of both 200 μs were applied. Silicon grease was used to provide coupling between the specimen surface and the AE sensors. According to ASTM E976-10 [34], pencil lead break is used for determining the reproducibility of acoustic sensors response. Three replicated tests were done to ensure experimental reliability for each type of FW composite tube. DIC cameras were also used to monitor the crushing process. The DIC system consists of two 5 MP 8-bit "Point Grey" cameras with "XENOPLAN 1.4/23" lenses, and VIC-Snap 8 software was used to record the speckle pattern images with an acquisition rate of 2 frames per second (fps) for the monotonic test. For processing, the subset size was set to 100×100 pixels with a step size of 7 pixels, and the observation window was approximately $120 \times 70\,\text{mm}^2$ which was equivalent to an image with dimensions of 2048×1194 pixels. The typical experimental setup of the axial compression testing of the composite tube is shown in Figure 2.

2.3.1. Clustering procedure

The second step for the assessment of damage mechanisms is partitioning the captured AE signals. Different unsupervised clustering models can be utilized for AE signals clustering. The operation of these techniques is partly on the structure of the AE dataset. The advantage of using these methods is the employment of multiples AE features simultaneously to differentiate different damage mechanisms. According to the literature, one of the techniques that give the optimized data clustering result is the hierarchical method. Data clustering with the hierarchical model is performed with the two forms of divisive and agglomeration. For both types of hierarchical methods, the data set A is partitioned into m sets $\{x_1, \ldots, x_n\}$ [35]. That is if subsets B_i and B_j satisfy that $B_i \in x_m$, $B_j \in x_l$ and $r \succ m$, then either $B_i \subset B_j$ or $B_i \cap B_j = 0$ for all $i \neq j$, $r, l = 1, \ldots, n$. In other words, there are two cases for two subsets of any hierarchical partition. One subset may completely contain the other, or they can completely disjoint. The divisive approach is the opposite of Agglomerative (Figure 3); it starts off with all the points into one cluster and divides them to create more clusters.

As can be seen from this figure, the clustering beginning with $k = N$ clusters and proceeds by merging the two closest classes into one cluster, obtaining $k = N - 1$ clusters. The process of merging two clusters to acquire $k - 1$ clusters is repeated until we attain the desired number of clusters. Also, to detect which clusters to amalgamate, the Euclidean and Cityblock distance is used.

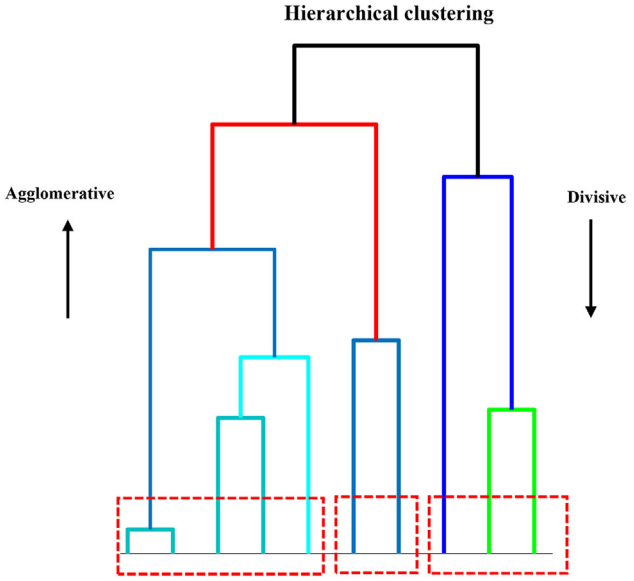

Figure 3. The dendrogram demonstration of the results of a hierarchical algorithm.

2.3.2. Wavelet analysis

In order to analyze the damage mechanisms and determine the percentage of each damage, it is necessary to utilize wavelet packet transform (WPT). Discrete Wavelet Transform (DWT) is one of the signal processing methods in which the primary signal is disjointed into two ingredients, and this process continues to the desired level [36, 37]. One of the methods that can be used to determine the appropriate level of signal decomposition is the entropy criterion. In the final step of decomposition, AE signals are decomposed into three levels and then divided into eight components [18, 35]. Then, according to Eq. (1), the energy percentage of eight disjointed components is obtained in the third level [18].

$$P_j^i(t) = c\sum_i \sum_j \frac{E_j^i(t)}{E_{\text{Total}}(t)} i = 1, \ldots, 2^j \tag{1}$$

Where $E_j^i(t)$ and $E_{Total}(t)$ are the energy level of each wavelet component and total energy of the signal, respectively, obtained by the following equations.

$$E_j^i(t) = \sum_{\tau=t_0}^{t} \left(f_j^i(\tau)\right)^2 \tag{2a}$$

$$E_{\text{total}}(t) = c\sum_i E_j^i(t) \tag{2b}$$

$f_1^i, \ldots, f_j^i$ represent each of the wavelet components for the ith level of decomposed signal, and $E_1^i, \ldots, E_j^i$ show the amount of energy associated with each component.

2.4. Crashworthiness indicators

There are various parameters to determine the energy absorption of composite tubes. Peak crushing force (*PCF*), energy absorption (EA=$\int_0^d F(x)dx$), specific energy absorption (SEA = EA/m), mean crushing force (F_{mean}=EA/d), and crushing force efficiency (CFE= F_{mean}/PCF) are some of these parameters [38, 39] used for this purpose. In these relations, F(x), d, m, and A show the instantaneous crushing force, crushing distance, mass, and cross-sectional area, respectively.

3. Numerical simulation

3.1. Modeling of FW composite tube

Figure 4 represents the flowchart of the proposed approach for creating a 3D FW composite tube pattern. As can be seen, FW composite tube is considered a combination of fiber roving and epoxy resin. For modeling of the tubes, first, the number of carbon fibers in the cross-section of the tube is calculated utilizing the fibers volume fraction and modeled with CATIA software. Then the matrix is modeled as a columnar membrane in ABAQUS software and the standard 3D winding composite is made by combining fibers and the epoxy resin. Afterward, the boundary conditions are applied to the 3D FW composite model subject to compressive loading.

3.2. Embedded method

The embedded element technique is considered for damage analysis and mechanical behavior of composite materials (Figure 5) [14]. In this method, the fibers and matrix properties of the FW composite tube are defined separately by user material subroutines. Then, the mechanical properties of the embedded area are updated at each stage of the failure analysis.

To simulate the fibers in CATIA software, the number of fibers is obtained in the cross-section of the FW composite tube [40]. According to Eq. (3), the hypothetical number of fibers in the square region is calculated in terms of four parameters [41].

$$N = \frac{XYZ\upsilon_f}{\pi ZR^2} = \frac{XY\upsilon_f}{\pi R^2} \tag{3}$$

where N, X, Y, and R are the number of fibers in the model space, the length of the model, the width of the model, and the radius of the fibers, respectively. Also, ν_f is the volume fraction of the filament fibers. First, the cross-section area of the FW composite tube with an inner radius of $R_i = 0.02875$ m, and an outer radius of $R_o = 0.03125$ m was calculated (Figure 6a, b). Then by considering the area of a 2D square surface equal to the actual cross-sectional area of the FW composite tube (Figure 6c), the number of fibers was obtained (Figure 6d–g). In Table 1, the dimensions of the square region and the total number of fibers are shown.

In the next step, through the generative shape design section, helix curves with specific dimensions are created in the clockwise and counterclockwise directions [$+\theta/-\theta$] in CATIA V5 software (Figure 6f). In total, 107 helices were made in a clockwise direction and 107 helices were designed in a counterclockwise direction. Also, the location of the existing fibers in the same direction was $\theta = 3.364°$ relative to each other. After designing the fibers in CATIA software, as shown

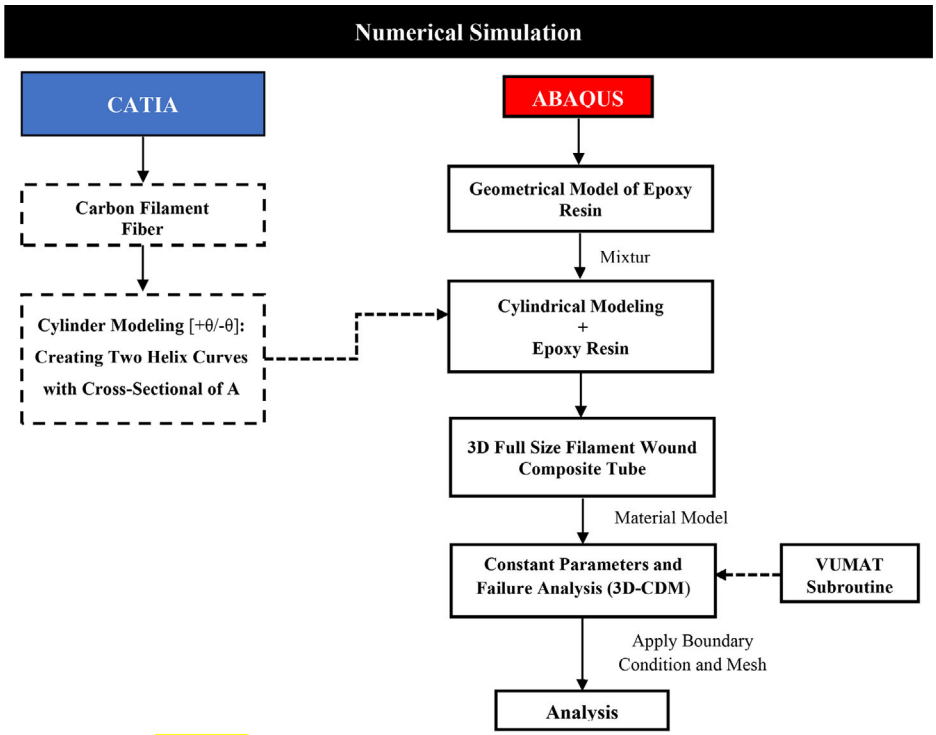

Figure 4. Simulation process for filament-wound composite tube.

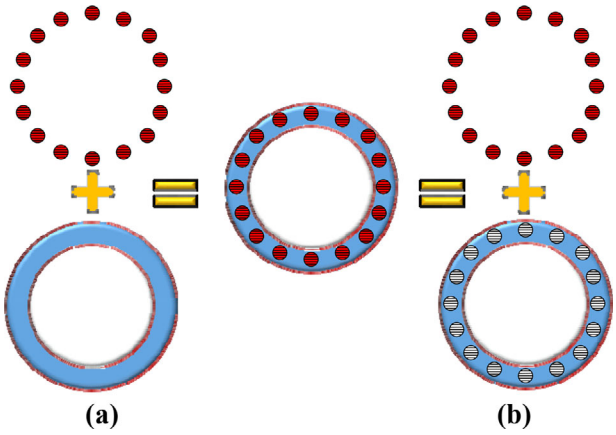

Figure 5. Schematic of the extra volume in the embedded method (a) A condition that is generally assumed in the software, and (b) The real state that simulate [14].

in Figure 6g, the fibers are entered into ABAQUS software and in the interaction section, are embedded by the embedding region tool inside a tubular host area which is considered as a matrix. After applying the material properties to the fiber and resin, the direction of the filament fibers is assigned to the local coordinate axes. Due to the non-linearity of material properties, boundary conditions, and structural geometry, an explicit solver was used during the analysis. The truss section type with a cross-section of 1.31mm^2 for the fibers and solid homogeneous section type was selected for the resin. The mesh type of resin was selected with 8-node linear brick elements with reduced integration and hourglass control (type C3D6R). The 2-node linear 3D elements (type C3D4) were used to mesh the fibers with appropriate inertial properties in order to put them inside the matrix. Boundary conditions of the bottom plate of the tube holder due to rigidity were defined as ENCASTRE during the experiment. The upper plate was only allowed to move in the axial direction. From the point of view of the interaction, the type of general contact was used between the holders and the tube. Self-contact was used to define the contact of different areas of the tube with each other during the test. The local coordinates defined for the composite tube in ABAQUS software are shown in Figure 7.

3.3. Material modeling

To assign the material properties and the damage criteria of woven fibers and resin, 3D user material subroutines were implemented for fibers wetted with resin during the manufacturing process. The relevant elements as interferes were defined by assigning a weaker mechanical property. Woven filamented roving consisting of matrix and filaments fiber is considered as a transversely isotropic composite material [42]. The resin was considered as an elastic-plastic material. The failure of polymeric resin was defined using the maximum stress criterion. For progressive damage analysis of the woven fibers, the 3D anisotropic plastic deformation model was used. ABAQUS explicit solver attached with user material subroutine (VUMAT) was employed to implement the progressive failure analysis. The Hill yield criterion for describing anisotropic plastic deformations [42, 43] was adopted as follows:

$$f(\sigma) = \sqrt{F(\sigma_{22}-\sigma_{33})^2 + G(\sigma_{33}-\sigma_{11})^2 + H(\sigma_{11}-\sigma_{22})^2 + 2L\sigma_{23}^2 + 2M\sigma_{31}^2 + 2N\sigma_{12}^2} \quad (4)$$

where F, G, H, L, M, and N are constants that are obtained as follows:

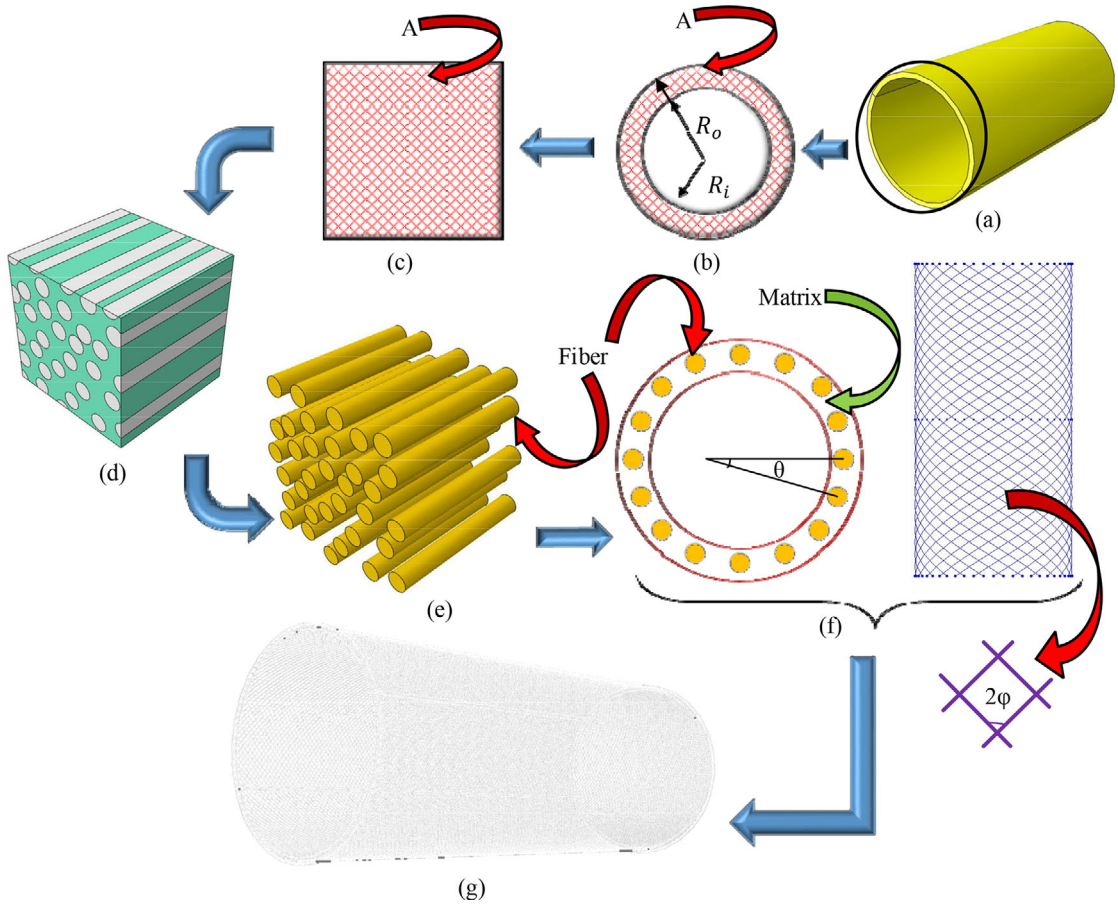

Figure 6. Schematic of a new approach designed for the analysis of filament wound composite tubes.

Table 1. Geometrical dimensions of square element.

Parameters	A (m^2)	X (m)	Y (m)	υ_f	N
Values	4.712×10^{-4}	0.0217	0.0217	59.48%	214

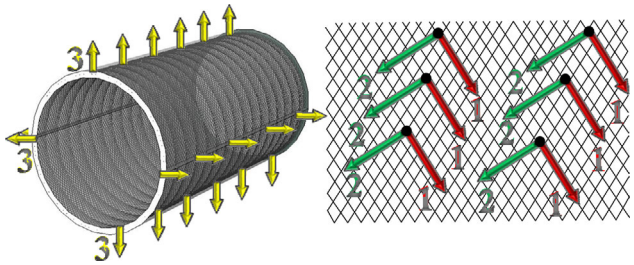

Figure 7. The coordinates of the FW composite tube.

$$F = \frac{\sigma_0^2}{2}\left(\frac{1}{\bar{\sigma}_{22}^2}+\frac{1}{\bar{\sigma}_{33}^2}-\frac{1}{\bar{\sigma}_{11}^2}\right) = \frac{1}{2}\left(\frac{1}{R_{22}^2}+\frac{1}{R_{33}^2}-\frac{1}{R_{11}^2}\right) \text{and}$$

$$R_{11} = \frac{\bar{\sigma}_{11}}{\sigma_0},\ R_{22} = \frac{\bar{\sigma}_{22}}{\sigma_0},\ R_{33} = \frac{\bar{\sigma}_{33}}{\sigma_0} \tag{5a}$$

$$G = \frac{\sigma_0^2}{2}\left(\frac{1}{\bar{\sigma}_{33}^2}+\frac{1}{\bar{\sigma}_{11}^2}-\frac{1}{\bar{\sigma}_{22}^2}\right) = \frac{1}{2}\left(\frac{1}{R_{33}^2}+\frac{1}{R_{11}^2}-\frac{1}{R_{22}^2}\right) \tag{5b}$$

$$H = \frac{\sigma_0^2}{2}\left(\frac{1}{\bar{\sigma}_{11}^2}+\frac{1}{\bar{\sigma}_{22}^2}-\frac{1}{\bar{\sigma}_{33}^2}\right) = \frac{1}{2}\left(\frac{1}{R_{11}^2}+\frac{1}{R_{22}^2}-\frac{1}{R_{33}^2}\right) \tag{5c}$$

$$L = \frac{3}{2}\left(\frac{\tau_0}{\bar{\sigma}_{23}}\right)^2 = \frac{3}{2R_{23}^2},\ R_{23} = \frac{\bar{\sigma}_{23}}{\tau_0} \tag{5d}$$

$$M = \frac{3}{2}\left(\frac{\tau_0}{\bar{\sigma}_{13}}\right)^2 = \frac{3}{2R_{13}^2},\ R_{13} = \frac{\bar{\sigma}_{13}}{\tau_0} \tag{5e}$$

$$L = \frac{3}{2}\left(\frac{\tau_0}{\bar{\sigma}_{23}}\right)^2 = \frac{3}{2R_{12}^2},\ R_{12} = \frac{\bar{\sigma}_{12}}{\tau_0} \tag{5f}$$

where $R_{11}, R_{22}, R_{33}, R_{12}, R_{23}$, *and* R_{23} are anisotropic yield stress ratios; σ_0 is the reference yield stress; each $\bar{\sigma}_{ij}$ is the measured yield stress value when σ_{ij} is exerted as the only nonzero stress component and $\tau_0 = \frac{\sigma_0}{\sqrt{3}}$.

4. Results and discussion

In the first section, the various failure modes corresponding to the force–displacement response of the two types of composite tubes were assessed by comparing surface damages during crushing history. The initiation of failure of progressive failure and catastrophic failure modes were detected using the AE method, and different failure mechanisms were separated using the machine learning based methods. Finally, the results of the 3D model were investigated. In Tables 2 and 3 the mechanical properties of fiber, epoxy resin, and FW woven fiber [42, 44] are shown.

Table 2. Mechanical properties of roving fibers and epoxy resin.

Parameters	$\rho\ (\frac{gr}{cm^3})$	$E_{11}\ (GPa)$	$E_{22} = E_{33}$	$\upsilon_{12} = \upsilon_{13}$	υ_{23}	$G_{12} = G_{13}$	$G_{23}\ (GPa)$	Tensile strength (MPa)
Fiber	1.78	230	14	0.25	0.3	9	5	3800–4000
Resin	1.17	3.1	–	0.3	–	0.89	–	85

Table 3. The mechanical properties of the FW woven fiber [42, 44].

Value		Parameter
Elastic properties	Longitudinal modulus E_{11} (*GPa*)	153.14
	$E_{22} = E_{33}$ (*GPa*)	9.5
	$G_{12} = G_{13}$ (*GPa*)	3.22
	G_{23} (*GPa*)	2.57
	Poisson's ratio $\nu_{12} = \nu_{13}$	0.25
	ν_{23}	0.3
Strength (MPa)	$\bar{\sigma}_{11}$ (MPa)	3200
	$\bar{\sigma}_{22} = \bar{\sigma}_{33}$ (MPa)	130
	$\bar{\sigma}_{23}$ (MPa)	86
	$\bar{\sigma}_{12} = \bar{\sigma}_{13}$ (MPa)	85
	σ_0 (MPa)	3200

4.1. Mechanical test results

The axial load–displacement curves and the DIC during crushing history are presented in Figure 8. As can be seen from the curves, all tubes had progressive crushing with high energy absorption and good reproducibility. As can be observed, the compression damage showed the progressive failure that begins at the top cross-section of the composite tubes. At the beginning crushing step of the experimental testing, the force rises to the maximum value and then drops to a small value. This attainable maximum load value was about 12.41, 12.4, and 12.35 kN, respectively, and the highest mean load of 11.06 kN was achieved for sample 1. Then, the axial load stands relatively constant with slight variation. This stage is crucial to measure crashworthiness parameters except for initial peak load and to understand failure mechanisms. As can be seen from damage history, at the beginning of loading, after destroying the chamfered area, the crushing force increased and caused the microcracks in the fiber's direction. Since the debonding stress applied on the specimen edge is less than the matrix strength, these cracks spread and the destruction of the sample is started. At this stage, in addition to the failure of the matrix, fiber failure also occurred and the composite tube was damaged with a special pattern. As can be observed from Figure 8, the compression damage showed the progressive failure that begins at the top cross-section of the composite tube, and as the loading progressed, matrix fragmentations followed by progressive folding occurred. In other words, the quasi-static force applied to the composite tubes caused the plies to bend in the form of a leaf from the stem (mode I), in and out of the specimen, and finally caused fractures along with the composite tubes. So, the results of experimental testing showed that creating a chamfer at one end of the tube improves the crashworthiness parameters, and leads to small fluctuations of loading around the mean crush load. The failure behavior of different specimens and crashworthiness indicators calculated from the load–displacement curves are presented in Tables 4 and 5. As can be seen, the failure behavior for all composite tubes follows a similar trend, and there is good repeatability between the calculated indicators. Also, the maximum force and the average force are not very different from each other, and as anticipated, the composite tubes are suitable for use as energy absorbers. Progressive damage mode shows the maximum load efficiency and energy absorption values as 89% and 738.3 J. Also, because of mass consideration, the specific energy absorption (SEA) in lieu of total energy must be prominent. The SEA values of these samples are 12.3, 12.14, and 10.97 J/g, respectively.

To compare the crashworthiness parameter of the FW composite tubes under compressive axial load in different damage modes (mode I and mode II), composite tubes without chamfer were tested. As can be seen from Figure 9, when mode II was dominant during the loading, the force first rised to 21.22 kN and then experienced a sudden drop. This maximum force level is considered undesirable for the impact resistance of a composite tube. In these specimens, it was observed that the macrocracks grew exactly along the fiber direction. It seems that due to the low fiber/matrix debonding stresses relative to the matrix strength, plastic deformation occurred at the buckling region. Therefore, the average crushing force was reduced by up to 35% (Table 6) compared to the progressive failure mode. This local buckling can be related to the matrix plastic behavior under high traction, and the diminutive interlayer tensions relevant to the strength of the matrix. Actually, the deformation around the buckling area is in the elastic region, whilst the buckling region experiences the non-uniform plastic deformation through the thickness. The convex side of the buckling region is under tension, while the concave side is under compression. Also, it seems that by changing the damage mode from mode I to mode II, the percentage of fiber failure decreased, and the failure rate of the matrix increased. In mode I, due to the direction of load application, part of the load is borne by the bridged fibers between the two plies, resulting in fiber failure, while in mode II loading, due to the application of in-plane shear load in the composite, most of the shear load applied to the matrix is tolerated and the fibers are subjected to lower load, which reduces the failure rate of the fibers relative to the matrix. As can be seen from Table 6, by changing the mode of tube failure from local buckling to ply bending mode, the energy absorption capacity increased to 448.42 J. Also, the specific energy absorption values of FW composite tubes for the progressive failure mode (7.47 J/g) were 2.57 times of catastrophic ones (2.91 J/g).

4.2. Simulation

In this section, the results of the numerical simulation of progressive damage mode are investigated. In Figure 10, the load–displacement curves related to the numerical method and experimental testing are shown. It can be seen that the numerical method can reasonably predict the linear behavior

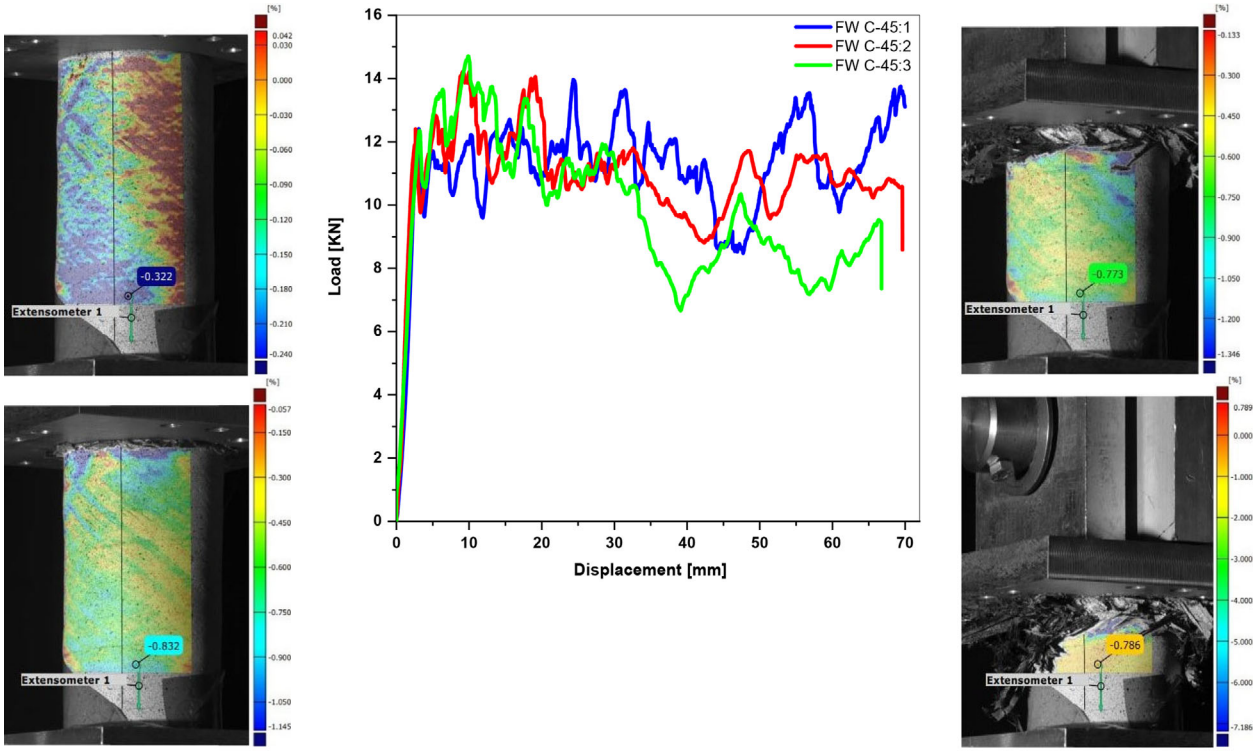

Figure 8. Force–displacement curve and DIC history of the FW composite tube under axial loading.

Table 4. Experimental results for crushing indicators in composite tubes under quasi-static loading.

Specimen	$EA = \int_0^d F(x)dx\ (J)$ 0to70mm	Standard deviation	$F_{mean}\,(kN)$	Standard deviation
C-45-1	738.3	35.48	11.06	0.53
C-45-2	728.75		10.92	
C-45-3	658.71		9.87	

Table 5. Experimental results for crushing indicators in composite tubes under quasi-static loading.

Specimen	PCF (kN) (Elastic region)	*CFE*	Fracture displacement (mm)	Maximum force in whole displacement (kN)
C-45-1	12.41	0.89	3.08	13.96
C-45-2	12.4	0.88	2.64	14.2
C-45-3	12.35	0.80	3.20	14.71

of maximum load and post-crushing values of the composite tube. However, there are also some subtle differences between the experimental testing and numerical simulation results in peak force prediction (1.64% discrepancy) and the obtained displacement for it. The results also indicate that the FE model can simulate the stiffness behavior well. The slope of the experimental diagram decreased earlier than the simulation diagram. In addition, suddenly descended of maximum load in the experimental testing curves is not observed in the numerical simulation diagram. There is also a good solidarity between the numerical simulation and experimental force–displacement diagrams until the displacement of 70 mm. The failure behavior of numerical and experimental results is shown in Table 7. As can be seen from this table, there is a good agreement between the proposed numerical model with experimental results in different crashworthy parameters, which is attributed to the adopted 3D modeling approach for the FW composite tubes. In order to analyze the associated damage morphology in the localized zones, the crushing steps of progressive damage mode are shown in Figure 11. According to the results of stress contour, the stress value of 3D woven fiber in the primary stages of loading was higher than that of the epoxy resin, and cause quicker amassing of plastic strain and failure in some zones. So, carbon fibers are more fragile compared with matrix resin at the primary steps. Then, transverse ply cracks, delamination, and fiber–matrix debonding appear and extend significantly with the increase of displacement. Also, it seems that the woven fiber experience plastic deformation earlier than the resin matrix, and there was no apparent shear damage characteristic of the epoxy resin. As can be seen, the FE model provided a good prediction of the mechanical response and damage morphology subjected to axial compression load.

4.3. Acoustic emission results

To identify the degradation and damage mechanisms in the FW composite tubes, AE signals were acquired during

loading. By analyzing the AE data using a machine learning method, different damage mechanisms were separated in the specimens. For this purpose, first, a statistical analysis based on a number of AE hits is performed to identify the best-received signals and at the same time to identify the amplitude distribution range. Based on the good reproducibility of the tests, only one curve for each type of sample is presented in this section. For the mechanical-acoustic coupling analysis, the AE energy, acoustic frequency, and cumulative AE energy for each failure mechanism are used to define the study regions. Figure 12a,b show the AE energy, cumulative AE events, and peak frequency versus the displacement curves of the FW composite tubes for progressive failure mode and catastrophic failure mode, respectively. Also, In Figure 12d, a diagram of the cumulative energy related to the failure of the matrix and the separation of the fibers from the matrix is plotted for progressive failure mode. As can be seen from this figure, the failure of fiber/matrix debonding occurred uniformly, while the failure of the matrix in some parts of the tube failure released a lot of energy, and caused a sharp increase in the curve. According to Figure 12c, by analyzing these acoustic emission parameters and matching the different regions of Figure 12a,b, five different representative regions are defined. In the first zone, configurations of two types of FW composite tubes report a displacement–load linear behavior. During this displacement interval, no acoustic activity is notable and the integrity of the FW composite tubes is maintained. The displacement intervals are 0.39 and 0.86 mm for progressive failure and catastrophic failure mode, respectively (Table 8). In the second part, there is a matrix cracking pattern that leads to minor damage, and low-energy AE events are observed in this zone. Irrespective of the initial AE events, the structure retains a linear behavior until the maximum patronaged load. The assessment of the frequency of the received signals at the beginning of this zone shows that the range is mainly between 130 and 190 kHz, and the energy level of these signals is very low. The cumulative AE energy of matrix cracking continues to increase till a specified stabilization begins at the end of the second region. With a difference of 59.05%, the displacement intervals for this acoustic stabilization are 1.05 mm for progressive damage mode and 1.67 mm for buckling mode (Table 8). In the third zone, fiber breakage takes place, so high-energy AE events are observed. This region is mainly accompanied by an increase in cumulative AE events, and new frequency changes happened within the range of 400–544 kHz. Then according to the frequency range of AE signals fiber/matrix debonding is initiated in 1.71 and 1.84 mm, respectively. With regard to Figure 12a,b, progressive damage mode generates more AE events that represent more pronounced fiber–matrix debonding and more fiber breakage during loading, which increases its structural stability. Also, the first high-energy AE event was

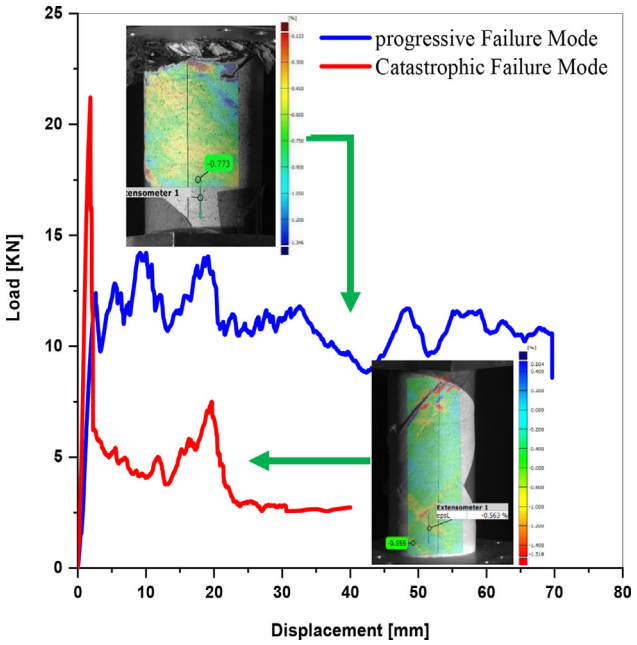

Figure 9. Force–displacement curve of the composite tube under axial loading for sample 2.

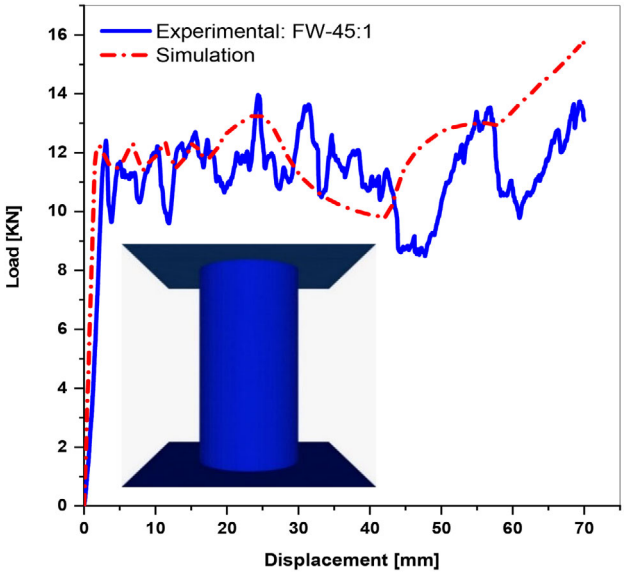

Figure 10. Displacement–force curves of composite tube for numerical method and experimental testing.

Table 7. Quantitative comparison of various parameter.

Parameter	Experimental	Numerical
PCF (*KN*)	12.41	12.21
EA (*J*)	738.3	812.1
$F_{mean}(kN)$	11.06	12.17
Fracture Displacement	3.08	2.23

Table 6. Quantitative comparison of the various parameters in mode I and mode II.

parameter	PCF (kN) (Elastic region)	$EA = \int_0^d F(x)dx$ (*J*) 0to40mm	$F_{mean}(kN)$	*CFE*	Fracture displacement (mm)	Maximum force (kN)
Progressive failure mode	12.4	448.42	6.72	0.54	2.64	14.2
Buckling	21.22	174.87	4.37	0.02	1.84	21.22

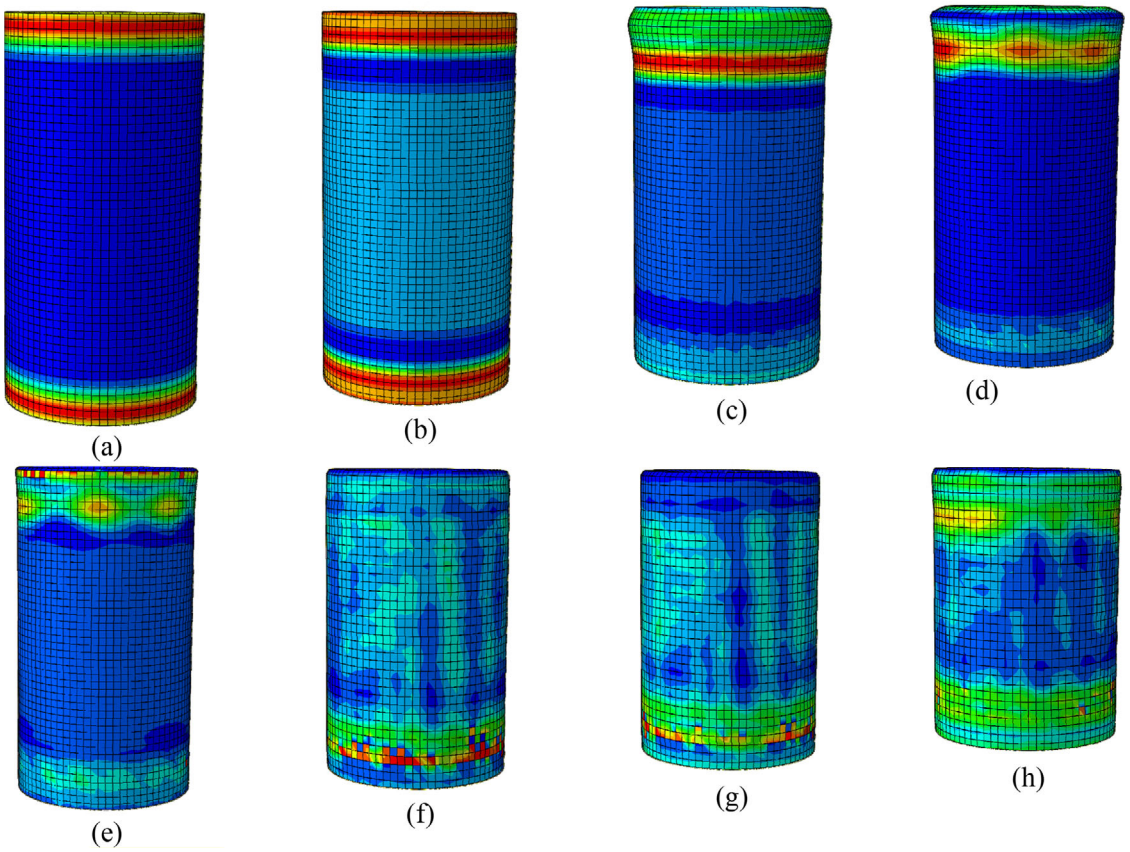

Figure 11. Stress distribution results of the numerical simulation approach.

started after dropping the displacement–load curve in peak elastic force. As can be seen from Figure 12b, in catastrophic failure mode, as the crack extends along the fibers and the load reaches its peak value, the percentage of matrix cracking increases dramatically. Then, because of fiber failure, intensive changes occur in the signal frequency, the level of energy released increases sharply, and the load suddenly decreases. In catastrophic failure mode, the maximum value of the released AE energy due to instantaneous fracture of the composite tube (8.79×108 eu) and severe force loss is higher than the progressive failure mode (5×107 eu), however, in progressive failure mode, the number of AE signals received is greater than the catastrophic failure state. Then, in the last zone, all of the damage mechanisms are activated in the FW composite tube. Region five shows the final failure scenario, and the failure of the FW composite tube tends to gradually continue with the accumulation of the AE events and gradual release of the AE energy. In this region, the frequency range of signals is associated with matrix cracking, debonding effects, and fiber breakage. Also, in catastrophic failure mode considering the AE activity recorded during this region with a constant cumulative AE energy, the damage continues its propagation in a fast manner. In Table 8, the received AE signals for progressive failure and catastrophic failure modes are shown in different displacements and forces. As can be seen from this table, in the progressive failure mode, the failure mechanisms are activated faster than in the buckling mode due to the presence of chamfer at the top of the FW composite samples.

The sentry function is defined as the logarithmic ratio of mechanical energy to the cumulative energy of AE [35]. Depending on the failure status in the loaded samples, four different trends of sentry function can be observed: (I) Incremental trend: this trend shows that there is no failure occurred in the samples. (II) Instantaneous decline: shows severe damage with high AE energy. (III) Gradual decreases: this process indicates microscopic failure such as matrix cracking. (IV) constant-state: shows the balance of mechanical failure and AE activity. The sentry function is expressed by the following equation [35]:

$$f(x) = \mathrm{Ln}\left[\frac{E_M(x)}{E_{AE}(x)}\right] \tag{5}$$

In Figure 13, the sentry function of the progressive failure mode and catastrophic failure mode was shown. For catastrophic failure mode, at the beginning of the curves, the sentry function shows the increasing trend (case I) followed by several continuous falls (instantaneous decline). These falls indicate the propagation of matrix cracking along the fiber direction, and subsequently fiber breakage, and finally create the local buckling mode. After this drop, the second kind of sentry function is apperceived which has a lower slope compared with the prime type. This shows that the stiffness of the FW composite tube was reduced. At a displacement of 2.08 mm, the sentry function curve slowly decreases, which represents that the acoustic energy is higher than the mechanical energy (Gradual decreases). Finally, with the increases in the displacement, the sentry

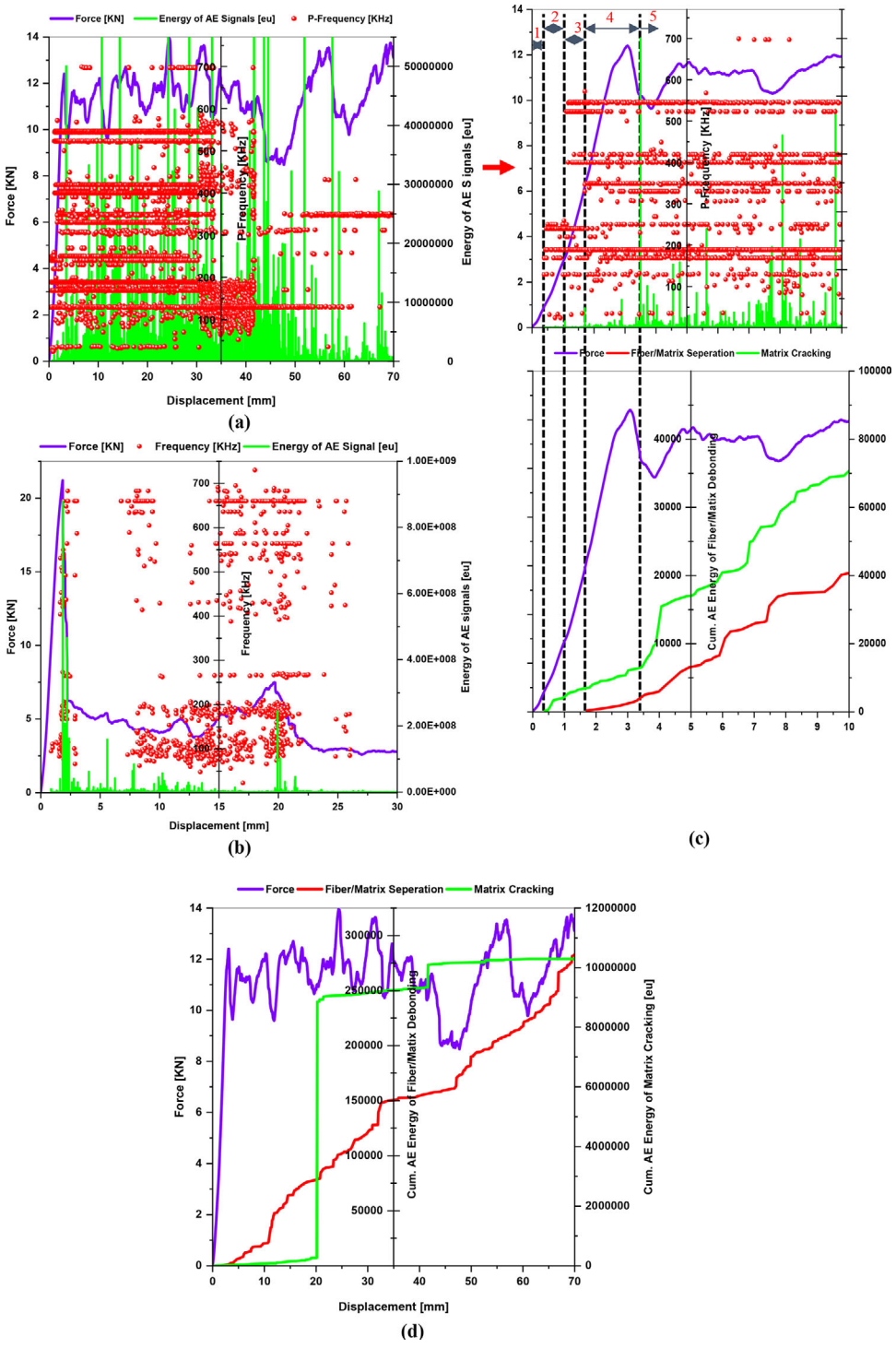

Figure 12. Energy of AE signal and peak frequency with respect to the displacement for (a) progressive failure mode, (b) catastrophic failure mode, (c) zoning the curves, and (d) Cumulative of AE energy for matrix cracking and fiber/matrix debonding.

Table 8. Characterization of the AE signal of composite tubes.

Parameters		Peak crushing force (PCF)	Propagation of micro-cracks	Fiber/matrix separation	Fiber breakage
Progressive damage	Displacement (mm)	2.64	0.39	1.71	1.05
	Force (KN)	12.4	0.91	6.3	2.97
	Percentage of maximum force	–	0.07	0.51	0.24
Buckling	Displacement (mm)	1.84	0.86	1.84	1.67
	Force (KN)	21.22	9.93	21.20	20.04
	Percentage	–	0.47	1	0.94

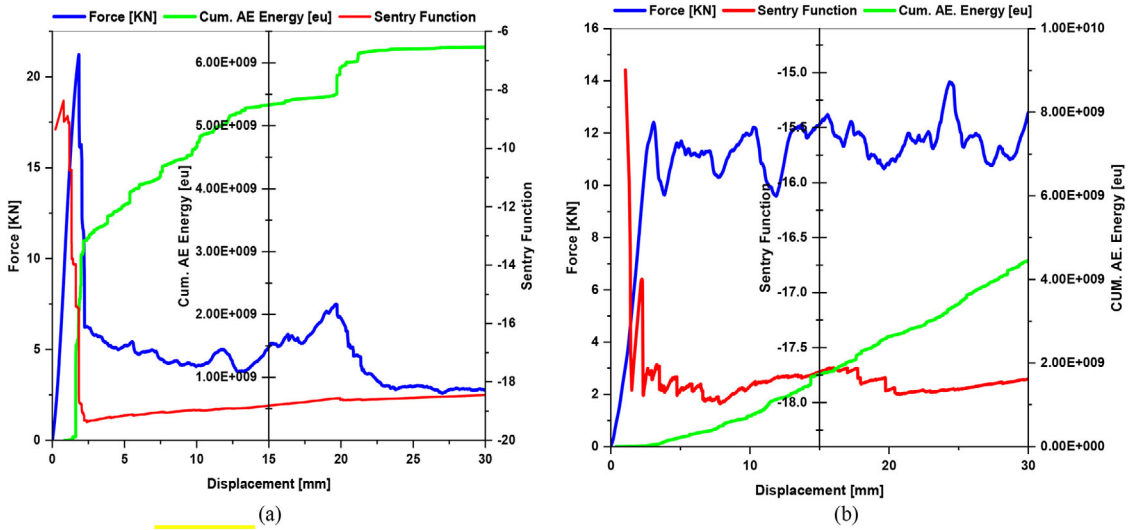

Figure 13. Sentry function behavior for (a) catastrophic failure and (b) progressive failure.

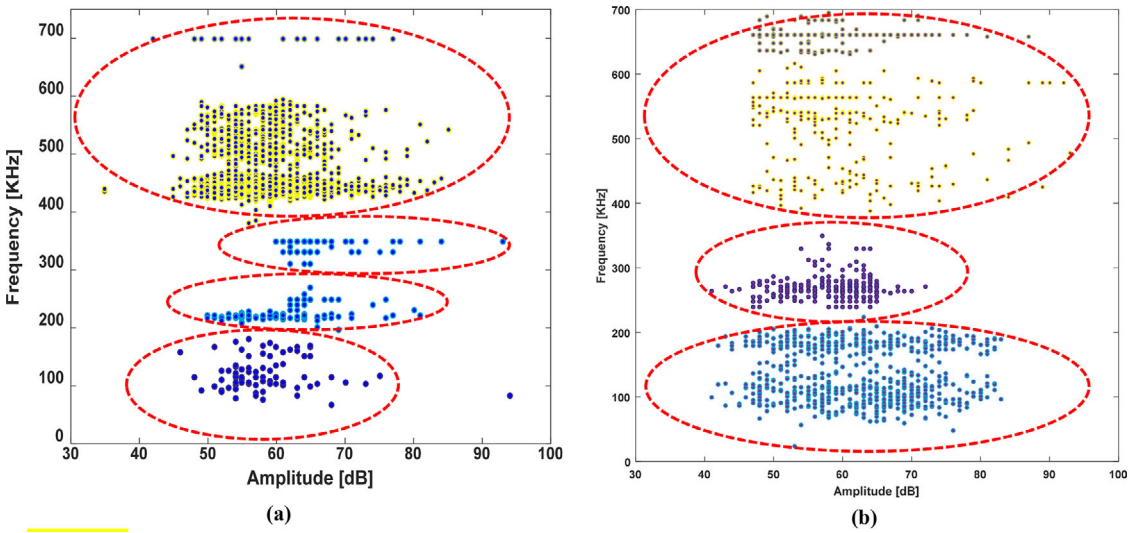

Figure 14. The hierarchical model classification for (a) progressive damage mode, and (b) catastrophic failure mode.

function shows a smooth behavior (stable-state), which represents an equilibrium between AE and strain energy. The behavior of the sentry function for different regions of the progressive failure mode is shown in Figure 13b. As can be seen from this figure to a displacement of 1.05 mm, no significant damage has occurred in the FW composite tube. At a displacement of 1.05 mm, with the occurrence of the first failures in the material, the sentry function drops sharply. There are several significant drops at the early stages of the sentry function curve. The first drop that contains several continuous drops could be considered as the first "significant" drop. Then, with the relative resistance of the material against the development of these failure mechanisms, the sentry function has an upward trend. However, as the strength of the material gradually decreases, the slope of the $f(x)$ function steadily decreases, to the point that at the displacement of 2.25 mm, which corresponds to the growth of fiber–matrix debonding and fiber breakage, the second sharp drop of the sentry function occurs. It seems that at this point the stiffness of the composite tube was decreased and the concavity of the curve changed, showing the effect of damage mechanisms on the stiffness reduction. After this sharp drop, the material resists damage propagation again, but as can be seen, the slope of the secondary $f(x)$ function is lower than the primary f function, which indicates a decrease in the material's resistance to damage. As can be seen from the curves, in the buckling mode at the beginning of loading, the cumulative energy curve grows uniformly, and suddenly increases near the maximum load with increasing failure mechanisms. But in progressive failure, the cumulative energy curve has experienced uniform changes. This indicates that by creating a chamfer on one side of the FW composite tubes we can improve the control of failure mechanisms. There is also a good correlation between the cumulative energy graph and the sentry function curve.

Due to the complex relations between the various parameters of AE, the clustering process of received signals is usually performed by machine learning-based methods. One of the methods for recognition of damage mechanisms is the

Table 9. Classification of the acoustic data with the hierarchical method.

Cluster No.		Matrix cracking	Fiber/matrix debonding	Delamination	Fiber breakage
Progressive failure mode	Amplitude (dB)	46–81	50–81	61–93	45–85
	Frequency (kHz)	68–200	200–270	310–350	>380
Catastrophic failure mode	Amplitude (dB)	41–84	<73	–	48–81
	Frequency (kHz)	54–224	240–350	–	>388

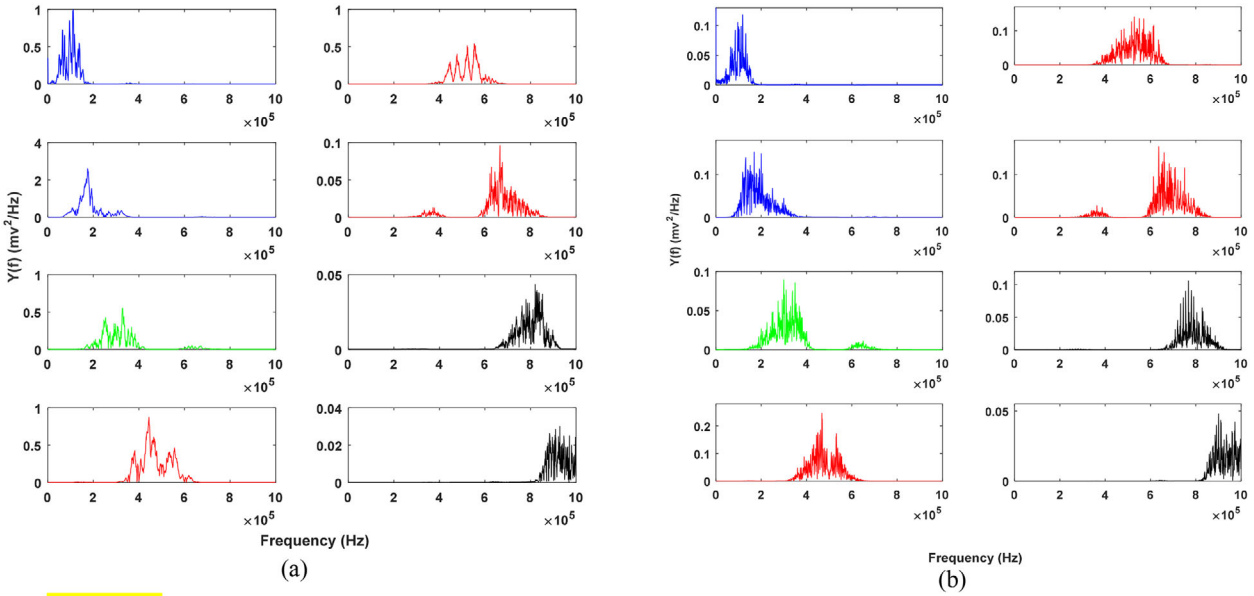

Figure 15. Fast Fourier Transform of the 3rd level WPT components for (a) progressive damage mode and (b) catastrophic mode.

use of unsupervised techniques. In this study, to map AE features into damage mechanism clusters during the compressive testing of the FW composite tube, which is based on the peak frequency and amplitude, an analysis procedure based on a hierarchical model was applied [35]. The utilized assessment procedure led to the identification of three clusters for catastrophic failure mode, and four clusters for progressive failure mode. As can be seen from Figure 14 in progressive failure mode, the signals related to the first cluster are characterized by amplitude between 46 and 81 dB, with frequencies from 68 to 200 kHz, respectively. The second and third clusters are characterized by an amplitudes range of 50–81 dB and 61–93 dB and a frequency range of 210–350 kHz, respectively. The fourth cluster is represented by the signals with an amplitude range of 45–85 dB, and a frequency over 380 kHz. Table 9 shows the amplitude and frequency range of the FW composite tubes for different failures in both progressive mode and catastrophic failure mode. As can be seen from the figures, it seems that in the catastrophic failure mode the received signals from the matrix cracking are very high, while in the progressive failure mode it is reduced and the density of the received signals due to the fiber breakage and the fiber–matrix separation is added. By comparing the received signals of progressive failure and catastrophic failure modes in the same frequency range of [200–350], it is clear that in the catastrophic failure mode the received signals are concentrated in the amplitude range of 41–73 dB, while in the progressive failure mode two types of signals are received in the amplitude range of 50–81 dB and 61–93 dB. It seems that in progressive failure mode these two ranges of received signals belong to different failure mechanisms. Examination of the morphology of the composite tubes under compressive load showed that due to the rapid degradation of the samples of mode II, fiber separation from the matrix occurred and delamination was observed to a very small extent. Actually, in catastrophic failure mode, the matrix failure occurs in the fiber direction, and in a region near the middle of the sample, it experiences local buckling. However, in the progressive failure mode due to plies bending, the failure starts from the top of the sample and continues in the form of petals with simultaneous delamination and fiber/matrix debonding. So, in the progressive failure mode, both fiber–matrix debonding and delamination occur simultaneously, but in the catastrophic failure mode, according to the failure occurred, the delamination seems negligible and the fiber–matrix debonding factor prevails. Also, the recognition between fiber–matrix debonding and delamination seems to be relatively challenging since both failure mechanisms report very similar frequency spectra. Research [25, 35] shows that the amplitude range of delamination signals is greater than the separation of fibers from the matrix. Therefore, it seems that the range of 50–81dB is related to the fiber–matrix debonding and the range of 61–93 dB is related to the delamination.

As explained in section 2.3.2, using the energy criterion, the energy percentage of each of the eight signal components decomposed in the third level is obtained. Each component has a specific frequency range depending on the level of decomposition at which it is located and whether

Table 10. The percentage of damage mechanisms obtained using WPT.

Sample type Percentage of damage mechanism (%)	Matrix cracking	Fiber/matrix debonding	Fiber breakage
Progressive damage mode	19.64	25.25	55.11
Catastrophic damage mode	71.17	6.433	22.397

the component is a high frequency or low frequency. By using the power spectrum analysis in the Fast Fourier Transform (FFT) approach, the decomposition of each of these components was carried out [18]. In Figure 15, the frequency range of each of the eight components was shown. According to the frequency range of eight components resulting from the decomposition of AE signals as well as the frequency range of matrix crack, fiber–matrix separation, and fiber breakage, the first and second components were dedicated to matrix cracking. Also, the third component and fourth, fifth, and sixth components were assigned to the separation between plies from the matrix and fiber breakage, respectively. Then, the energy percentage of each decomposed component was calculated using the energy criterion [18], and the percentage of each failure mechanism in the composite tube was obtained, as presented in Table 10. For the catastrophic failure mode, the dominant mechanism of failure seems matrix cracking. As the change of mode state to progressive damage, the fiber breakage and fiber–matrix debonding percentage increases, and the matrix cracking percentage decreases. It seems that the best energy absorption in a structure is controlled by the fiber/matrix debonding, delamination, and fiber breakage. In other words, a structure that has high energy absorption should generally absorb a large percentage of energy by these two failure mechanisms. In other words, other damage mechanisms frequently cause a sharp drop in the force–displacement curves and are not considered favorable for energy absorption. As shown in Table 10, the WPT results confirm the above proposition.

5. Conclusion

In this research, the crashworthiness characteristics and the involved failure mechanisms of two types of FW composite tubes subjected to quasi-static axial compression were assessed through experimental testing, AE monitoring, and numerical simulation. The WPT approach together with an unsupervised pattern recognition method was used to classify and process the AE signals and estimate the contribution of damage mechanisms, dominant failure mechanisms, and their relationship with the type of failure modes. Furthermore, a FE model of 3D FW composite tubes with the help of the embedded region method and the volume fraction of fibers was proposed to analyze the crashworthiness characteristics and damage behavior of the composite tubes. The results obtained from this research study are summarized below:

1. To use the full potential of FW composite tubes one must be able to set the stiffness and buckling performance using suitable design parameterization to better exploit crashworthy characteristics and postpone buckling, as shown here.
2. Analysis of the damage patterns, and the displacement and strain fields of DIC, indicated that mode II composite tubes are dominated by local buckling, which led to longitudinal crack propagation due to the plastic deformation. Whereas in mode I composite tubes ply bending happened and subsequently reached material failure mainly due to matrix cracking, delamination, debonding, and fiber breakage.
3. By changing the failure mode from catastrophic failure to progressive damage mode, the fiber/matrix separation and the fiber breakage increases, and the contribution percentage of matrix cracking decreases. The evaluation of failure mechanisms indicated that the cause for the large drop in the load at catastrophic mode is mainly the propagation of the matrix cracking in the fibers' direction. Therefore, the catastrophic mode will absorb a lower amount of energy.
4. In the progressive failure mode, both fiber/matrix debonding (50–81 dB) and delamination (61–93 dB) occur simultaneously, but in the catastrophic failure mode, the delamination seems negligible and the fiber/-matrix debonding (<73) factor prevails.
5. Synchronous examination of mechanical and the AE results showed that the response of two types of failure modes (mode I and mode II) to the loading includes five zones so that each load drop in the experimental curves was related to considerable released energy of AE signals.
6. The specific energy absorption values of FW composite tubes for the progressive failure mode (7.47 J/g) were about 2.5 times of catastrophic ones (2.91 J/g).
7. It seems that a quantitative assessment of each failure mechanism can be of great help to improve the crashworthiness efficiency of the structure by controlling the content of each damage.
8. It was found that the FE model can effectively predict the mechanical response and damage morphology of the composite tubes.

Acknowledgements

The author(s) received no financial support for the research, authorship, and/or publication of this article.

References

[1] W. Guan, and G. Gao, Crashworthiness analysis of shrink circular tube energy absorbers with anti-climbers under multiple loading cases, Mech. Adv. Mater. Struct., pp. 1–17, 2022. DOI: 10.1080/15376494.2022.2033892.

[2] Z. Zhang, W. Sun, Y. Zhao, and S. Hou, Crashworthiness of different composite tubes by experiments and simulations, Compos. Part B. Eng., vol. 143, pp. 86–95, 2018. DOI: 10.1016/j.compositesb.2018.01.021.

[3] H. Han, F. Taheri, and N. Pegg, Crushing behaviors and energy absorption efficiency of hybrid pultruded and ±45° braided tubes, Mech. Adv. Mater. Struct., vol. 18, no. 4, pp. 287–300, 2011. DOI: 10.1080/15376494.2010.506103.

[4] C. J. McGregor, R. Vaziri, A. Poursartip, and X. Xiao, Simulation of progressive damage development in braided composite tubes under axial compression, Compos. Part A Appl. Sci. Manuf., vol. 38, no. 11, pp. 2247–2259, 2007. DOI: 10.1016/j.compositesa.2006.10.007.

[5] Y. Gu, D. Zhang, Z. Zhang, J. Sun, S. Yue, G. Li, and K. Qian, Torsion damage mechanisms analysis of two-dimensional braided composite tubes with digital image correction and X-ray micro-computed tomography, Compos. Struct., vol. 256, pp. 113020, 2021. DOI: 10.1016/j.compstruct.2020.113020.

[6] G. Ryzińska, M. David, G. Prusty, J. Tarasiuk, and S. Wroński, Effect of fibre architecture on the specific energy absorption in carbon epoxy composite tubes under progressive crushing, Compos. Struct., vol. 227, pp. 111292, 2019. DOI: 10.1016/j.compstruct.2019.111292.

[7] H. Luo, Y. Yan, X. Meng, and C. Jin, Progressive failure analysis and energy-absorbing experiment of composite tubes under axial dynamic impact, Compos. Part B Eng., vol. 87, pp. 1–11, 2016. DOI: 10.1016/j.compositesb.2015.10.016.

[8] H. Luo, X. Li, Y. Li, X. He, J. Ye, and Z. Li, Damage properties of pre-embedded connection of carbon fiber wound composite tubes, Mater. Today Commun., vol. 25, pp. 101525, 2020. DOI: 10.1016/j.mtcomm.2020.101525.

[9] R. Rafiee, M. A. Torabi, and S. Maleki, Investigating structural failure of a filament-wound composite tube subjected to internal pressure: experimental and theoretical evaluation, Polym. Test., vol. 67, pp. 322–330, 2018. DOI: 10.1016/j.polymertesting.2018.03.020.

[10] D. Shi, and X. Xiao, An enhanced continuum damage mechanics model for crash simulation of composites, Compos. Struct., vol. 185, pp. 774–785, 2018. DOI: 10.1016/j.compstruct.2017.10.084.

[11] R. Higuchi, T. Okabe, A. Yoshimura, and T. Tay, Progressive failure under high-velocity impact on composite laminates: Experiment and phenomenological mesomodeling, Eng. Fract. Mech., vol. 178, pp. 346–361, 2017. DOI: 10.1016/j.engfracmech.2017.03.019.

[12] M. Esa, P. Xue, M. Zahran, M. Abdelwahab, and M. Khalil, Novel strategy using crash tubes adaptor for damage levels manipulation and total weight reduction, Thin-Walled Struct., vol. 111, pp. 176–188, 2017. DOI: 10.1016/j.tws.2016.11.018.

[13] V. G. Belardi, P. Fanelli, and F. Vivio, Structural analysis and optimization of anisogrid composite lattice cylindrical shells, Compos. Part B Eng., vol. 139, pp. 203–215, 2018. DOI: 10.1016/j.compositesb.2017.11.058.

[14] A. Şık, E. Gürses, and B. Sabuncuoglu, Development of a procedure to model the mechanical behavior of composites with embedded element method by considering the matrix non-linearity, Compos. Struct., vol. 259, pp. 113400, 2021. DOI: 10.1016/j.compstruct.2020.113400.

[15] H. Shen, Z. Tang, Y. Su, J. Liu, D. Yu, and R. Zhang, Characteristics of wave propagation, vibration transmission and acoustic emission in fluid-filled coaxial periodic shells, Mech. Adv. Mater. Struct., vol. 27, no. 3, pp. 196–208, 2020. DOI: 10.1080/15376494.2018.1472335.

[16] M. Saeedifar, J. Mansvelder, R. Mohammadi, and D. Zarouchas, Using passive and active acoustic methods for impact damage assessment of composite structures, Compos. Struct., vol. 226, pp. 111252, 2019. DOI: 10.1016/j.compstruct.2019.111252.

[17] A. Fernández, F. J. Rescalvo, A. Cruz, C. Abarkane, and J. M. Santiago, Acoustic emission analysis of raw bamboo subjected to tensile tests, Mech. Adv. Mater. Struct., vol. 28, no. 13, pp. 1389–1397, 2021. DOI: 10.1080/15376494.2019.1675105.

[18] F. Mohamad, H. Hossein, P. Farzad, and M. Ahmadi Najaf Abadi, Composite materials damage characterization under quasi-static 3-point bending test using fuzzy C-means clustering, Appl. Mech. Mater., vol. 110, pp. 1221–1228, 2012.

[19] D. Ranz, J. Cuartero, L. Castejón, and R. Miralbes, A study on interlaminar behavior of carbon/epoxy laminated curved beams by use of acoustic emission, Mech. Adv. Mater. Struct., vol. 27, no. 18, pp. 1609–1618, 2020. DOI: 10.1080/15376494.2018.1522559.

[20] N. Beheshtizadeh, and A. Mostafapour, Processing of acoustic signals via wavelet & Choi-Williams analysis in three-point bending load of carbon/epoxy and glass/epoxy composites, Ultrasonics., vol. 79, pp. 1–8, 2017. DOI: 10.1016/j.ultras.2017.04.001.

[21] E. H. Saidane, D. Scida, M.-J. Pac, and R. Ayad, Mode-I interlaminar fracture toughness of flax, glass and hybrid flax-glass fibre woven composites: Failure mechanism evaluation using acoustic emission analysis, Polym. Test., vol. 75, pp. 246–253, 2019. DOI: 10.1016/j.polymertesting.2019.02.022.

[22] H. Q. Ali, I. E. Tabrizi, R. M. A. Khan, A. Tufani, and M. Yildiz, Microscopic analysis of failure in woven carbon fabric laminates coupled with digital image correlation and acoustic emission, Compos. Struct., vol. 230, pp. 111515, 2019. DOI: 10.1016/j.compstruct.2019.111515.

[23] A. Huijer, C. Kassapoglou, and L. Pahlavan, Acoustic emission monitoring of carbon fibre reinforced composites with embedded sensors for in-situ damage identification, Sensors., vol. 21, no. 20, pp. 6926, 2021. DOI: 10.3390/s21206926.

[24] M. B. Ameur, A.E. Mahi, J.-L. Rebiere, I. Gimenez, M. Beyaoui, M. Abdennadher, and M. Haddar, Investigation and identification of damage mechanisms of unidirectional carbon/flax hybrid composites using acoustic emission, Eng. Fract. Mech., vol. 216, pp. 106511, 2019. DOI: 10.1016/j.engfracmech.2019.106511.

[25] M. Šofer, J. Cienciala, M. Fusek, P. Pavlíček, and R. Moravec, Damage analysis of composite CFRP tubes using acoustic emission monitoring and pattern recognition approach, Materials, vol. 14, no. 4, pp. 786, 2021. DOI: 10.3390/ma14040786.

[26] A. B. Khalifa, M. Zidi, and L. Abdelwahed, Mechanical characterization of glass/vinylester ±55 filament wound pipes by acoustic emission under axial monotonic loading, C. R. Méc., vol. 340, no. 6, pp. 453–460, 2012. DOI: 10.1016/j.crme.2012.02.006.

[27] A. Rabiee, and H. Ghasemnejad, Progressive crushing of polymer matrix composite tubular structures, OJCM., vol. 07, no. 01, pp. 14–48, 2017. DOI: 10.4236/ojcm.2017.71002.

[28] L. Pickett, and V. Dayal, Effect of tube geometry and ply-angle on energy absorption of a circular glass/epoxy crush tube – A numerical study, Compos. Part B Eng., vol. 43, no. 8, pp. 2960–2967, 2012. DOI: 10.1016/j.compositesb.2012.05.040.

[29] G. Lu, and T. X. Yu, Energy Absorption of Structures and Materials, Elsevier, New York, USA, 2003.

[30] H. W. Song, X. W. Du, and G. F. Zhao, Energy absorption behavior of double-chamfer triggered glass/epoxy circular tubes, J. Compos. Mater., vol. 36, no. 18, pp. 2183–2198, 2002. DOI: 10.1177/0021998302036018515.

[31] Y. Ren, H. Jiang, and Z. Liu, Evaluation of double- and triple-coupled triggering mechanisms to improve crashworthiness of composite tubes, Int. J. Mech. Sci., vol. 157–158, pp. 1–12, 2019. DOI: 10.1016/j.ijmecsci.2019.04.024.

[32] S. Alimirzaei, M. A. Najafabadi, A. Nikbakht, and L. Pahlavan, Damage mechanism characterization of ±35° and ±55° FW composite tubes using acoustic emission method, Int. J. Dam. Mech., vol. 31, no. 8, pp. 1230–1253, 2022.

[33] ASTM D2584-18, Standard test Method for Ignition Loss of Cured Reinforced Resins, ASTM International, West Conshohocken, PA, USA, vol. 8.01, pp. 3, 2018.

[34] ASTM E976-10, Standard Guide for Determining the Reproducibility of Acoustic Emission Sensor Response, ASTM

International, West Conshohocken, PA, USA, vol. 03.03, pp. 7, 2015.

[35] M. Saeedifar, and D. Zarouchas, Damage characterization of laminated composites using acoustic emission: a review, Compos. Part B Eng., vol. 195, pp. 108039, 2020. DOI: 10.1016/j.compositesb.2020.108039.

[36] C. K. Chui, Wavelets: A Tutorial in Theory and Applications, Academic Press Professional, Inc., San Diego, USA, 1993.

[37] G. A. Oliver, J. L. J. Pereira, M. B. Francisco, and G. F. Gomes, The influence of delamination parameters on the wavelet based damage index in CFRP structures, Mech. Adv. Mater. Struct., pp. 1–11, 2022. DOI: 10.1080/15376494.2022.2028204.

[38] B. Natarajan, S. Subramaniam, P. NavaneethaKrishnan, D. Karupannasamy, S. Chinnasamy, and S. Rajagopal, Augmentation of crashworthiness design of circular tubular structures by engraving grooves of varying depths, Mech. Adv. Mater. Struct., pp. 1–14, 2022. DOI: 10.1080/15376494.2022.2069307.

[39] S. Alimirzaei, M. A. Najafabadi, and A. Khodaei, Characterization of the damage mechanism of glass/epoxy composite tubes under quasi-static axial loading using acoustic emission monitoring, Appl. Compos. Mater., vol. 29, no. 5, pp. 11911–1936, 2022.

[40] H. Ma, and X.-L. Gao, A three-dimensional Monte Carlo model for electrically conductive polymer matrix composites filled with curved fibers, Polymer, vol. 49, no. 19, pp. 4230–4238, 2008. DOI: 10.1016/j.polymer.2008.07.034.

[41] M. I. Okereke, and A. I. Akpoyomare, A virtual framework for prediction of full-field elastic response of unidirectional composites, Comput. Mater. Sci., vol. 70, pp. 82–99, 2013. DOI: 10.1016/j.commatsci.2012.12.036.

[42] T. Liu, X. Wu, B. Sun, W. Fan, W. Han, and H. Yi, Investigations of defect effect on dynamic compressive failure of 3D circular braided composite tubes with numerical simulation method, Thin-Walled Struct., vol. 160, pp. 107381, 2021. DOI: 10.1016/j.tws.2020.107381.

[43] R. Hill, On discontinuous plastic states, with special reference to localized necking in thin sheets, J. Mech. Phys. Solids, vol. 1, no. 1, pp. 19–30, 1952. DOI: 10.1016/0022-5096(52)90003-3.

[44] Z. Pan, X. Wu, and L. Wu, Temperature rise caused by adiabatic shear failure in 3D braided composite tube subjected to axial impact compression, J. Compos. Mater., vol. 54, no. 10, pp. 1305–1326, 2020. DOI: 10.1177/0021998319877558.